Supplementary material for: The Max Planck CloudKite (MPCK): High-Resolution Airborne Measurements of Turbulence and Cloud Microphysics

Gholamhossein Bagheri[1], Freja Nordsiek[1], Oliver Schlenczek[1], Yewon Kim[1], Birte Thiede[1], Venecia Chávez-Medina[1], Philipp Höhne[1], Torben Neumann[1], and Eberhard Bodenschatz[1,2,3]

[1]Max Planck Institute for Dynamics and Self-Organization (MPI-DS), Am Faßberg 17, 37077 Göttingen, Germany
[2]Institute for Dynamics of Complex Systems, Georg-August University of Göttingen, Friedrich-Hund-Platz 1, 37077 Göttingen, Germany
[3]Laboratory of Atomic and Solid State Physics and Sibley School of Mechanical and Aerospace Engineering, Cornell University, 130 Upton Hall, Ithaca NY 14853, USA

Correspondence: Gholamhossein Bagheri (gholamhossein.bagheri@ds.mpg.de) and Eberhard Bodenschatz (eberhard.bodenschatz@ds.mpg.de)

1 Supplementary Text

1.1 Theoretical Detection Holography Design Considerations

Let λ_h be the illumination wavelength, w_h the pixel width (assuming square pixels), and M_h the magnification. The x- and y-axes define the camera plane, with the z-axis normal to it. The camera has $N_{h,x}$ and $N_{h,y}$ pixels in each direction, and the effective pixel size is w_h/M_h. The imaging plane is $L_{h,z}$ from the illumination exit window. This means that the lateral dimensions of the view volume are $L_{h,x} = N_{h,x}w_h/M_h$ and $L_{h,y} = N_{h,y}w_h/M_h$. Then view volume V_h is then

$$V_h = L_{h,x}L_{h,y}L_{h,z} = \frac{N_{h,x}N_{h,y}w_h^2}{M_h^2}L_{h,z} \quad . \tag{S1}$$

The choice of reconstruction method also puts a hard lower bound on the resolution.

This is how such a holography system can give the seemingly counter-intuitive result of resolving a USAF 1951 test target down to where the line thickness is about a pixel, but this is actually to be expected since the line triplet pattern itself is about 5 pixels across at this size and therefore easy to distinguish from noise.

Besides the pixel size, the other hard lower bound on the resolution is the diffraction limit from the effective sensor size in the imaging plane. If we consider a particle of diameter/width d, the maximum distance from the hologram plane it can be resolved at $z_{max}(d)$ is where the frequency spatial $1/d$ is undersampled/underresolved. Since the sensor is a rectangle, the limiting frequency is different in different directions, but the shortest dimension limits the resolution most. From Fugal et al. (2009)'s Eq. 13 and 14 (note, there is a typo where the expression on the right hand side of each should be taken to the power of $-1/2$ instead of -2), the smallest sensor dimension leads to a $z_{max}(d)$ of

$$
\begin{aligned}
z_{max}(d) &= \frac{d w_h \min\left(N_{h,x}, N_{h,y}\right)}{2 M_h \lambda_h} \sqrt{1 - \frac{\lambda_h^2}{d^2}} \\
&\simeq \frac{d w_h \min\left(N_{h,x}, N_{h,y}\right)}{2 M_h \lambda_h}
\end{aligned} \tag{S2}
$$

where we have used $d \gg \lambda_h$ since we are considering minimum d of at least a few micrometers and $\lambda_h \leq 532$ nm. Re-arranging, the diffraction limit for the smallest diameter that can be resolved $d_{h,min,diff}(z)$ is

$$
d_{h,min,diff}(z) \simeq \frac{2 M_h \lambda_h z}{w_h \min\left(N_{h,x}, N_{h,y}\right)} \tag{S3}
$$

Let z_r be the depth where the two resolution limits are equal, which is

$$
z_r \simeq \frac{w_h^2 \min\left(N_{h,x}, N_{h,y}\right)}{M_h^2 \lambda_h^2} \tag{S4}
$$

Combining the two limits, the resolution on the smallest objects that can be seen at a given distance $d_{h,min}(z)$ is

$$
d_{h,min}(z) \geq \begin{cases} \frac{2 w_h}{M_h} & \text{if } z \leq z_r \\ \frac{2 M_h \lambda_h z}{w_h \min\left(N_{h,x}, N_{h,y}\right)} & \text{if } z > z_r \end{cases} \tag{S5}
$$

where the $\geq$ comes from the fact that equality is the theoretical best and that the optical and sensor imperfections of real systems make the performance worse. For a particular d, it is possible for $z_{max}(d) < L_{h,z}$ in which case the maximum effective view volume $V_{h,eff}$ is less than the V_h. As with $d_{h,min}$, the actual effective view volume can be smaller due to imperfections in the optical system. The effective view volume as a function of d is

$$
V_{h,eff}(z) \leq \begin{cases} 0 & \text{if } d < \frac{2 w_h}{M_h} \\ \frac{d w_h^3 N_{h,x} N_{h,y} \min\left(N_{h,x}, N_{h,y}\right)}{2 M_h^3 \lambda_h} & \\ & \text{if } \frac{2 w_h}{M_h} \leq d < \frac{2 M_h \lambda_h L_{h,z}}{w_h \min\left(N_{h,x}, N_{h,y}\right)} \\ \frac{N_{h,x} N_{h,y} w_h^2 L_{h,z}}{M_h^2} & \text{otherwise.} \end{cases} \tag{S6}
$$

To get the total sample rate, we need to consider the speed of the camera, which depends mostly on the maximum rate that pixels can be read and streamed off the camera $\mathcal{P}_h$ and the resolution. The maximum frame rate f_h is inherently limited by $f_h \leq \mathcal{P}_h / N_{h,x} N_{h,y}$, and is often within a factor of two of the limit. If we consider a camera operating at its limit, the volumetric sampling rate $\mathcal{V}_h$ is

$$\mathcal{V}_h = f_h V_{h,eff}(z) \leq \begin{cases} 0 & \text{if } d < \frac{2w_h}{M_h} \\ \frac{d\, w_h^3 \mathcal{P}_h \min(N_{h,x}, N_{h,y})}{2 M_h^3 \lambda_h} & \\ & \text{if } \frac{2w_h}{M_h} \leq d < \frac{2 M_h \lambda_h L_{h,z}}{w_h \min(N_{h,x}, N_{h,y})} \\ \frac{\mathcal{P}_h w_h^2 L_{h,z}}{M_h^2} & \text{otherwise.} \end{cases} \tag{S7}$$

From here, the choices were made to optimize a balance of minimizing the lowest detectable size $2w_h/M_h$, maximizing the view volume depth $\min(L_{h,z}, z_{max}(d))$, maximizing the total sample rate $\mathcal{V}_h$, and minimizing the distance between successive holograms for any particular airspeed (maximizing f_h). Given the weight and size constraints for the MPCK$^+$, the maximum $L_{h,z}$ was in the 20–30 cm range. Decreasing λ_h increases $\mathcal{V}_h$ by both increasing $V_{h,eff}$ for sizes where $z_{max}(d) < L_{h,z}$ and decreasing maximum size that is affected by the diffraction limit, and doesn't negatively impact the other quantities though optical and safety concerns to prevent making it arbitrarily small. We chose to use $\lambda_h = 355$ nm since that is the smallest λ_h that can be used with standard glass and plastic lenses and their AR coatings, the quantum efficiency of many camera sensors drops off very rapidly after or even before 355 nm, and going further into the UV (like 265 nm) would have meant difficulty with staying under the laser damage thresholds of the optics, dealing with solarization of the optics, and the light becoming more hazardous. Also, using 355 nm makes it much easier to filter out sunlight with a bandpass filter since the solar illumination on Earth's surface at 355 nm, the part that would get through the passband, is much less than at say 532 nm.

The lowest detectable size scales linearly with the effective pixel size w_h/M_h, but $\mathcal{V}_h$ scales quadraticly or cubicly with it meaning that any choice helps and hurts at least one quantity that is trying to be optimized. We chose an effective pixel size of ≈ 3 µm in order to reliably detect and size particles with $d \geq 10$ µm (being at least 3 pixels across makes detection more reliable) and resolve down to a similar minimum size as HOLODEC II (Beals, 2013b, a; Beals et al., 2015) and HALOHolo (Schlenczek, 2018; Glienke et al., 2020). Going smaller would have very negatively affected $\mathcal{V}_h$.

mode with internal storage) was ≈ 2Gpx/s via quad CXP-6 (CoaXPress). The monochrome On Semi PYTHON25K CMOS sensor (5120×5120 pixels, 4.5µm, max $f_h = 80$ Hz) was selected as it offered $\mathcal{P}_h = 2.10$ Gpx/s—among the highest available. Many quad CXP-6 cameras supported this sensor, largely due to its continuity with the On Semi VITA25K.

Key advantages included a global shutter for short exposures (ensuring a bright hologram over background sunlight), a square format maximizing $\mathcal{V}h$ by optimizing $\min(Nh,x, N_{h,y})$, a moderate sensor diagonal (32.6mm) allowing weak magnification ($M_h = 1.5$) and ease of low-distortion lens selection, and sufficient SNR for ≈ 8-bit light level resolution per pixel. Additionally, its resolution, $N_{h,x} = N_{h,y} = 5120 = 2^{10} \times 5$, consists of small prime factors (2 and 5), enabling efficient FFT processing on GPUs. The quantum efficiency at 355nm was 18

For the camera, we used the SVS-VISTEK HR25000MCX (M58 mount), which operated down to -10 °C and provided a more stable mount than common F-mounts. Incidentally, the frame's pixel count was a multiple of 512, allowing efficient zero-copy IO on the acquisition computer via direct memory access(DMA).

In order to make it possible to have overlapping holograms and PIV images, we use $f_h = 75$ Hz which is only a bit lower than the maximum. After choosing the approximate PIV volume size and trying to reduce weight, $L_{h,z}$ ended up being 21.9 cm.

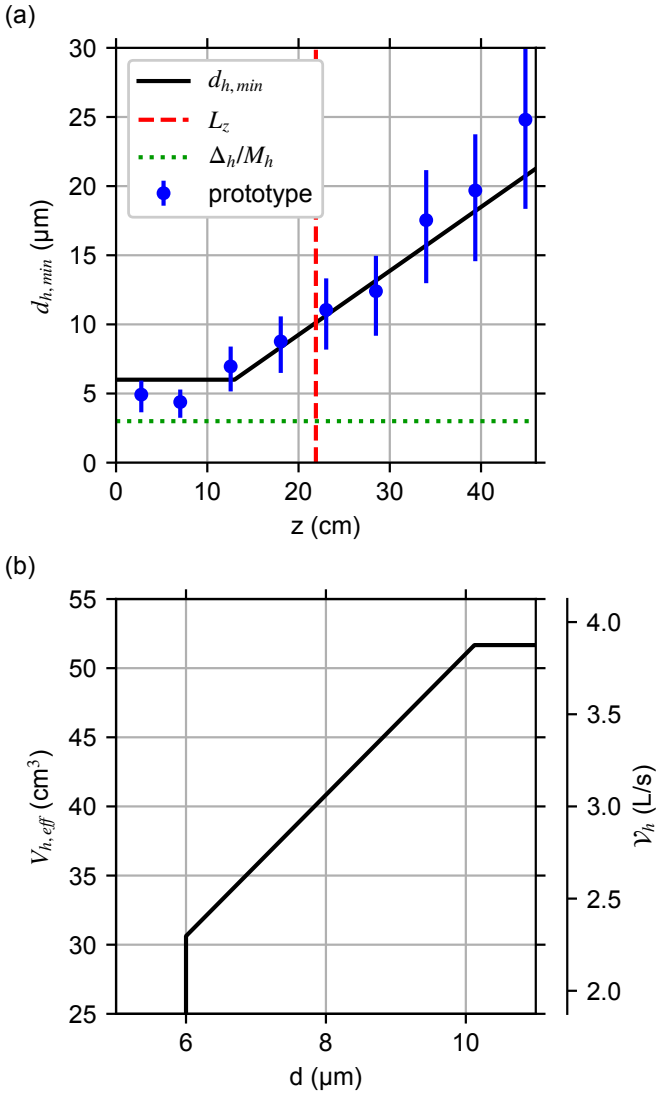

Figure S1. (a) Theoretical best case for the minimum resolvable particle size $d_{h,min}$ (Eq. S5) for the MPCK$^+$'s holography system at different distances z from the hologram plane along with resolutions determined for the prototype holographic system using a USAF 1951 test target (see Figure S10) with error bars denoting ± 2 elements on the target. The vertical dashed red line denotes the length of the holography view volume $L_{h,z}$, and the horizontal dotted green line denotes the effective pixel size. (b) Theoretical best cases for the effective view volume per hologram $V_{h,eff}$ (Eq. S6) and volumetric sampling rate $\mathcal{V}_h$ (Eq. S7) of the MPCK$^+$'s holography system for different spherical particle diameters d.

For these parameters; the theoretical ideal values of $d_{h,min}(z)$, $V_{h,eff}(d)$, and $\mathcal{V}_h(d)$ are shown in Fig. S1 along with the resolutions determined using a USAF 1951 test target on the prototype holography system (same optics except a different and worse collimating lens and the optical system was setup on an optical table instead of in its frame see Figure S10). The smallest particles that can be seen no matter where in the view volume they are is $d = 10.1$ µm, with the view volume reducing for smaller sizes. At the smallest resolvable size of 6 µm, the view volume is reduced by about 40% ($z_r = 13.0$ cm, which is $z_r/L_{h,z} = 0.593$). The volumetric sampling rate is quite high with a minimum of 2.30 L/s (8.27 m^3/hr) for $d = 6$ µm and going up to 3.88 L/s (13.95 m^3/hr) for $d \geq 10.1$ µm. The resolutions determined for the prototype holography system match up well with the diffraction limit and, as expected, at close range settle to between the 1 effective pixel feature size limit and 2 effective pixel object size limit.

1.2 Euler angle and velocity measurement correlation for tether-mount configuration

In this section, we present the stability of the MPCK$^+$with the tether-mount configuration during the Pallas Cloud Experiment (PaCE 2022)Schlenczek et al. (2025) field campaign. Among the three Euler angles, the yaw angle is largely determined by the wind direction and speed at the Helikite altitude and is therefore not considered in detail. Figure S2 shows pitch angle histograms and Figure S3 shows corresponding histograms for the roll angle. The pitch angle variability is generally small, with a full width at half maximum (FWHM) typically below 5°, indicating stable platform behaviour in tether-mount configuration. The median pitch angle remained slightly positive throughout most flights, which is advantageous for the imaging unit as it minimizes the influence of the instrument tips on the spatial distribution of cloud droplets. After a tether-mount adjustment during the campaign, the median roll angle was reduced to around 1°, reflecting improved platform stability.

The frequency spectra of the Euler angles provide additional insight into potential platform motion effects. We performed power spectral analysis for seven PaCE 2022 flights (Figure S4) and compared the results with wind speed spectra from the 1D pitot tube (Figure S5). Distinct dominant frequencies between 0.05 and 0.5 Hz were consistently observed in both pitch and roll angles, corresponding to spatial scales of approximately 10–200 m. The wind speed spectra generally followed Kolmogorov scaling, except for one flight affected by instrumental noise. Notably, the dominant frequencies in the Euler angles and wind speed largely overlapped (0.1–1 Hz), suggesting a common origin, likely related to platform motion.

We further examined the relationship between the dominant frequencies in the Euler angle spectra and relative turbulence intensity (standard deviation divided by mean wind speed). A clear negative correlation ($r^2 = -0.65$) was found between turbulence intensity and the pitch angle dominant frequency, while the roll angle showed a positive correlation ($r^2 = 0.50$). The pitch–wind speed correlation varied across flights, with stronger negative correlations (r^2 between -0.27 and -0.71) in the early flights and weaker correlations (r^2 between -0.06 and -0.11) in the later flights, reflecting improved platform balance. Correlations between roll angle and wind speed were generally weak ($|r^2| < 0.1$).

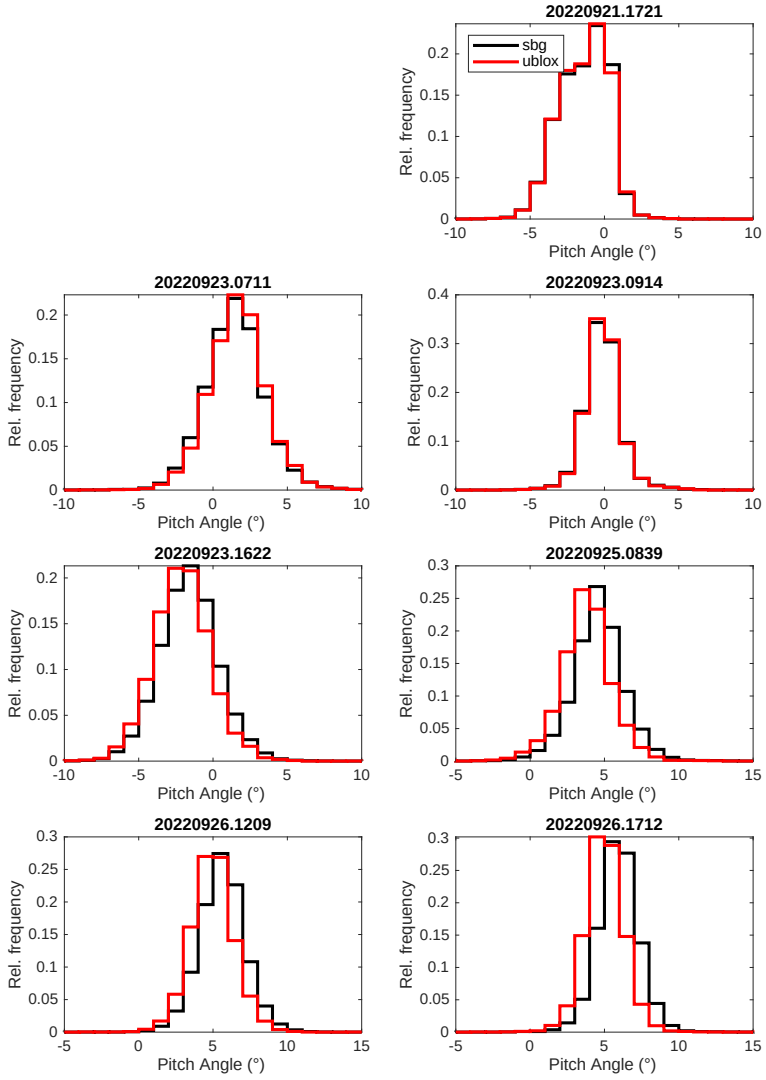

Figure S2. Histograms of MPCK$^+$pitch angle in tether-mount configuration during seven flights of the PaCE 2022 field campaign. The flight number is given in the title, the black line represents the SBG data while the red line represents the ublox data. Data were restricted to at least 50 m altitude above ground.

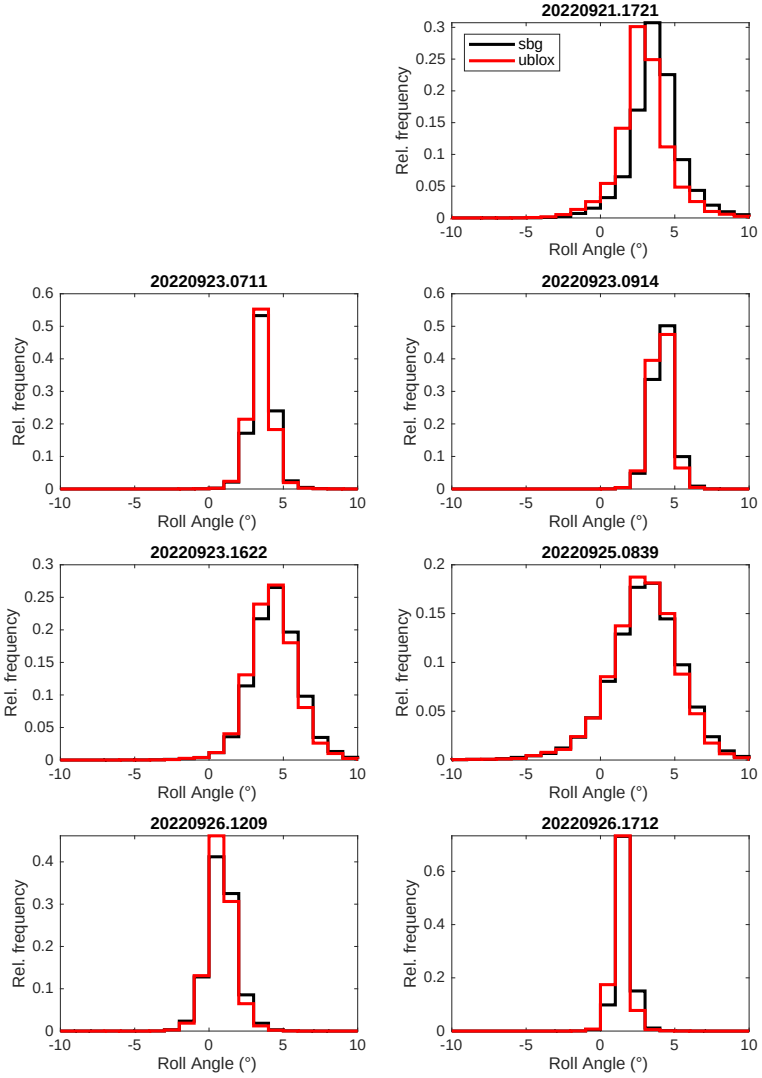

Figure S3. As in Figure S2 for the MPCK^{+}roll angle.

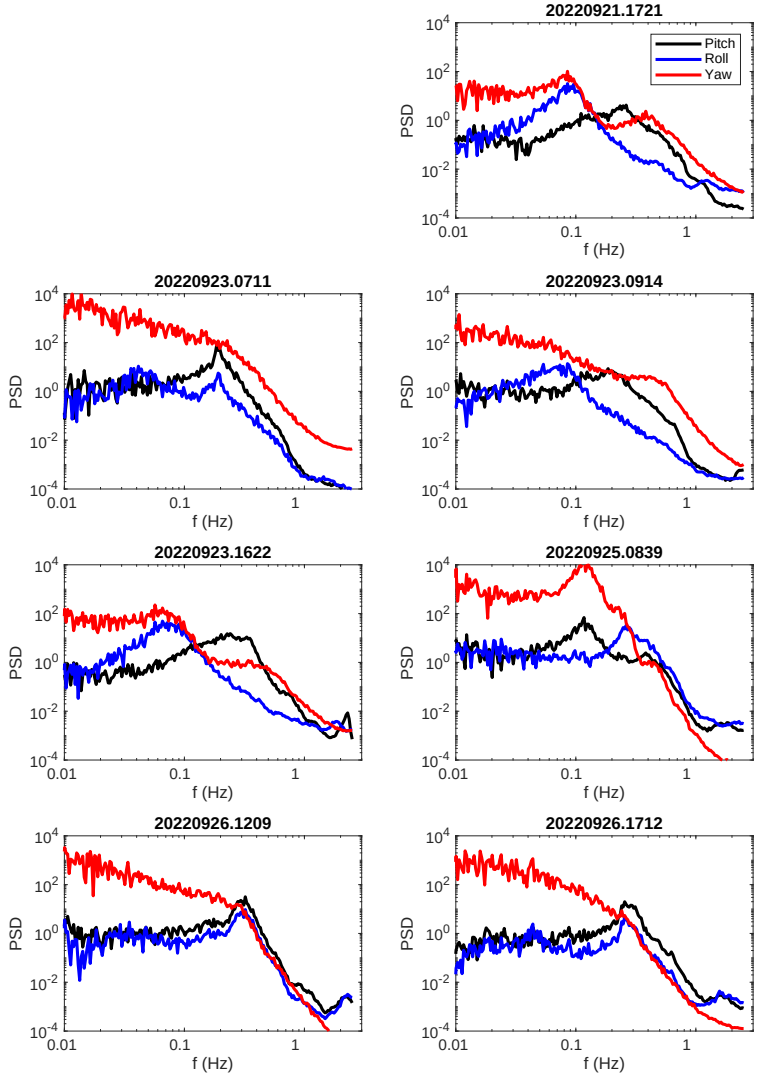

Figure S4. Power spectral density as a function of frequency for the three Euler angles measured during seven flights of PaCE 2022.

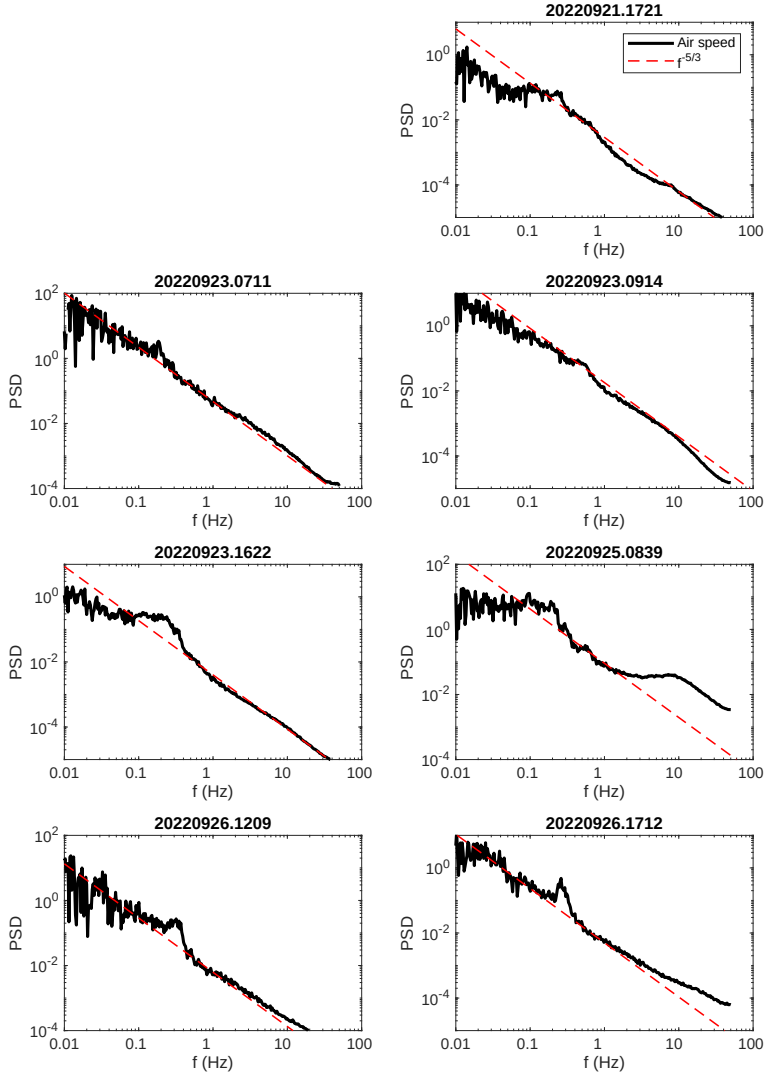

Figure S5. As in Figure S4 for the wind speed measured with the PSS8 unit. In addition to the power spectra, the fitted power law with the -5/3 slope for the Kolmogorov scaling law is plotted as dashed red lines.

2 Supplementary Figures

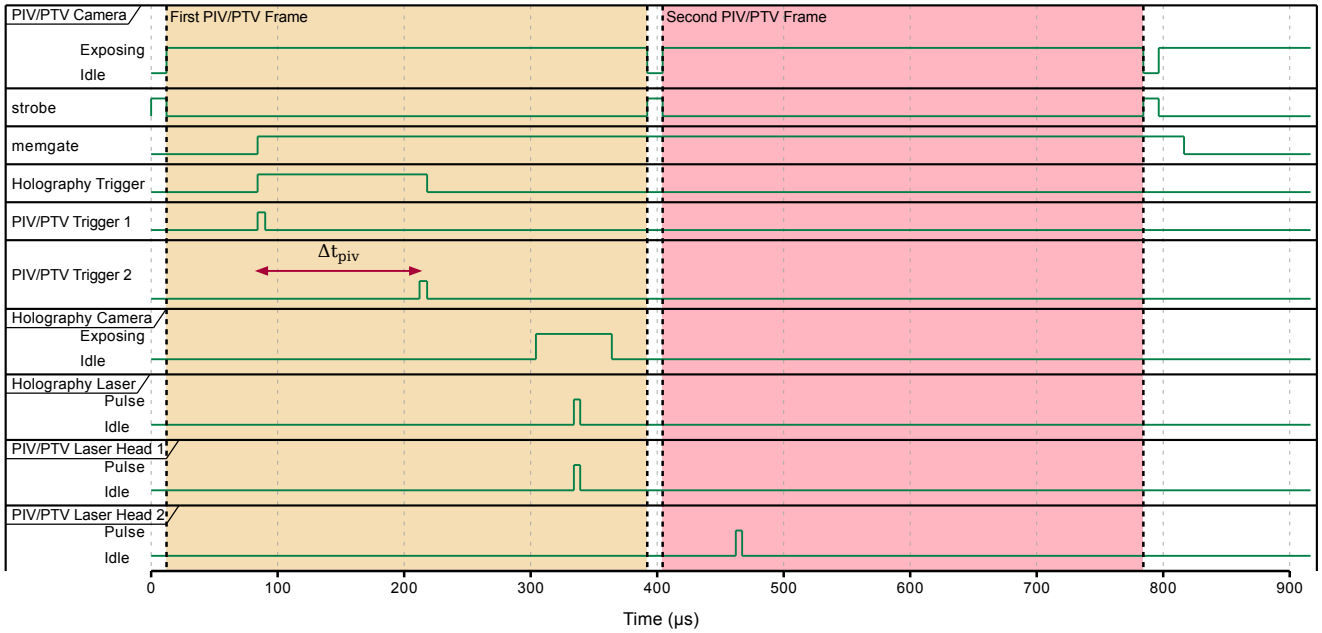

Figure S6. Timing diagram for the Particle Imaging system on a frame when both the PIV and holography systems are triggered. The pair of exposures from the PIV camera that are saved are highlighted. The length of the laser pulses themselves are exaggerated to make them more visible.

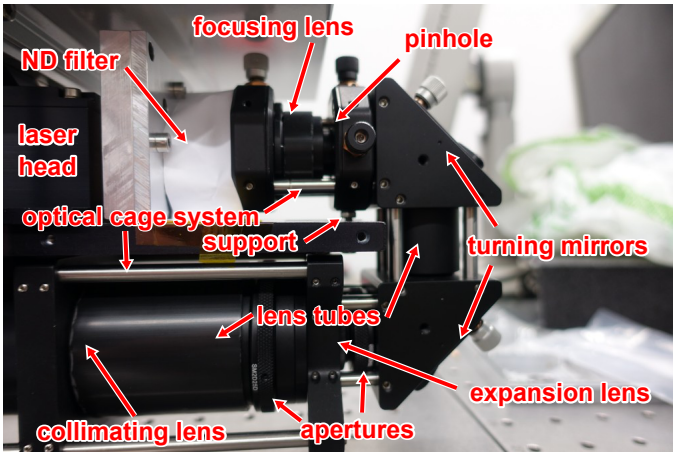

Figure S7. Picture with labels of the first optics of the laser side of the holography system where the spatial filter, folding turning mirror assembly, and expansion and collimation optics are.

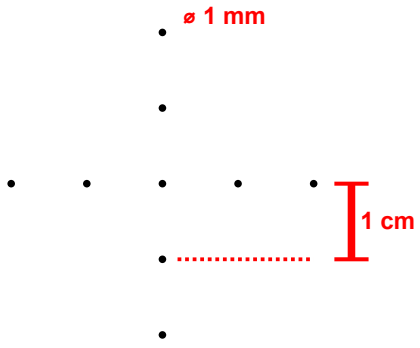

Figure S8. Diagram of the hole pattern in the mask used to check the collimation of the holography system, with labels for the hole separation and diameter. The diagram is to scale.

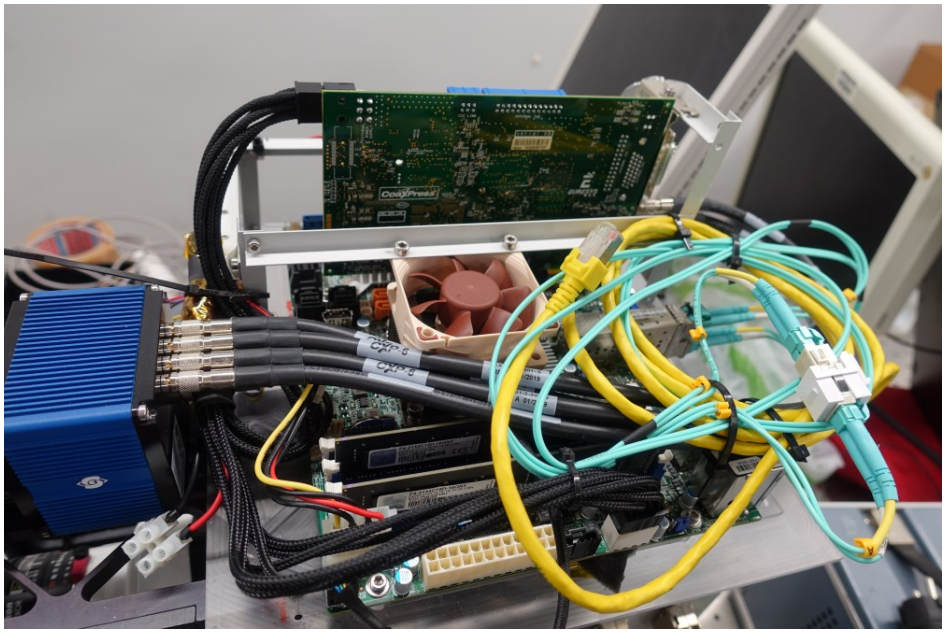

(a)

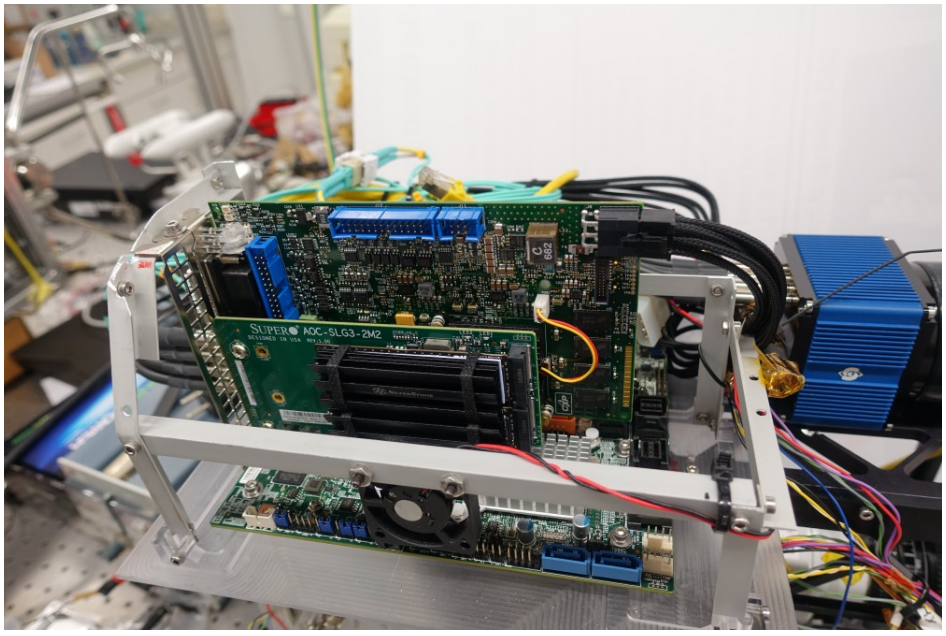

(b)

Figure S9. The holography computer from (a) the CPU/camera side and (b) the PCIe card side.

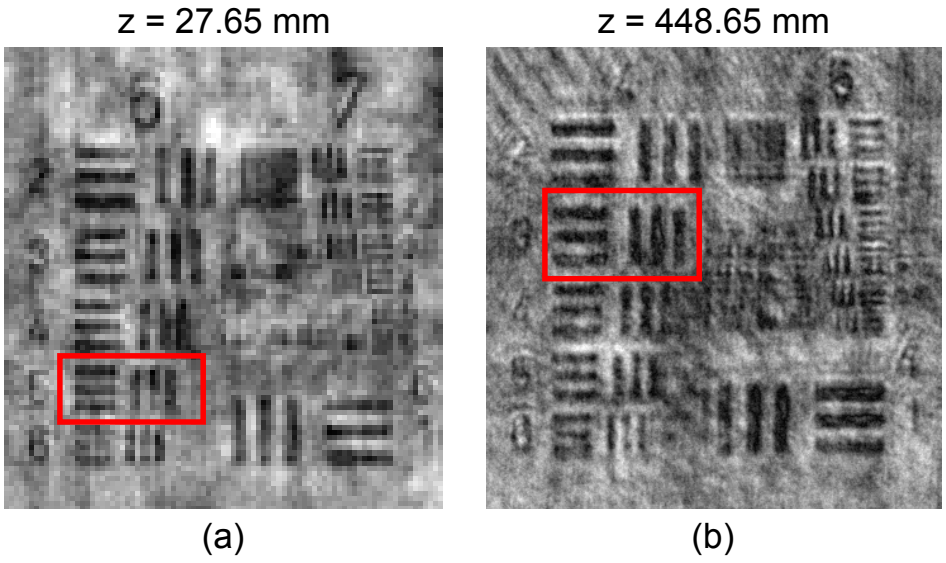

Figure S10. Reconstructed slices of the USAF 1951 test target for when it was at its (a) closest and (b) furthest distances from the camera, cropped to the part of the test target where the resolution was determined. The reconstructed distances are indicated above the slices. The identified group-element pair manually determined to be the resolution is surrounded by a red box.

3 Additional Tables

Table S1. The mean (denoted by $\langle\cdot\rangle$) and standard deviation (denoted by σ) of the particle diameters of Thermo Scientific Duke Standard 9000 Series glass microspheres from the manufacturer's calibration certificate and holograms taken with the MPCK$^+$prototype holography system and HALOHalo. N is the number of particles recorded. For the means, the 95% confidence interval from the manufacturer (includes both sample and instrument uncertainties) and two times the standard deviation in the mean for the instruments (95% confidence interval just for the sample uncertainties) are listed. For the standard deviations, the 95% confidence intervals for the instruments just from sample uncertainties are listed (intervals are small enough compared to the values that they can be approximated as $\pm$ a number as opposed to writing both end points). HALOHalo data is from Bagheri et al. (2021).

Nominal	Manufacturer		MPCK$^+$			HALOHolo		
d (µm)	$\langle d\rangle \pm 95\%$CI (µm)	σ_d (µm)	N	$\langle d\rangle \pm 2\sigma_{\langle d\rangle}$ (µm)	$\sigma_d \pm 95\%$CI (µm)	N	$\langle d\rangle \pm 2\sigma_{\langle d\rangle}$ (µm)	$\sigma_d \pm 95\%$CI (µm)
8	7.7 ± 0.4	1.0	234	7.82 ± 0.19	1.46 ± 0.13	467	7.79 ± 0.15	1.61 ± 0.10
10	9.8 ± 1.0	1.2	234	9.90 ± 0.26	1.98 ± 0.18	611	9.16 ± 0.17	2.04 ± 0.11
15	14.4 ± 0.8	1.8	197	14.76 ± 0.22	1.55 ± 0.15	538	14.32 ± 0.17	1.97 ± 0.12
20	20.2 ± 1.2	2.8	111	21.77 ± 0.53	2.81 ± 0.38	596	19.40 ± 0.19	2.29 ± 0.13
30	29.5 ± 1.0	1.9	247	30.51 ± 0.21	1.67 ± 0.15	334	30.18 ± 0.20	1.84 ± 0.14
40	42.3 ± 1.1	1.5	248	43.36 ± 0.14	1.12 ± 0.10	149	42.87 ± 0.21	1.26 ± 0.14
50	49.3 ± 1.4	3.4	249	50.61 ± 0.21	1.66 ± 0.15	217	49.61 ± 0.27	1.97 ± 0.19

References

Bagheri, G., Schlenczek, O., Turco, L., Thiede, B., Stieger, K., Kosub, J.-M., Pöhlker, M. L., Pöhlker, C., Moláček, J., Scheithauer, S., and Bodenschatz, E.: Exhaled particles from nanometre to millimetre and their origin in the human respiratory tract, medRxiv, https://doi.org/10.1101/2021.10.01.21264333, 2021.

Beals, M. J.: THE HOLOGRAPHIC DETECTOR FOR CLOUDS FROM TRL 5 TO TRL 8, Master's report, Michigan Technological University, http://digitalcommons.mtu.edu/etds/694, 2013a.

Beals, M. J.: Investigations of Cloud Microphysical Response to Mixing Using Digital Holography, Ph.D. thesis, Michigan Technological University, ISBN 9781303736155, http://digitalcommons.mtu.edu/etds/669, 2013b.

Beals, M. J., Fugal, J. P., Shaw, R. A., Lu, J., Spuler, S. M., and Stith, J. L.: Holographic measurements of inhomogeneous cloud mixing at the centimeter scale, Science, 350, 87–90, https://doi.org/10.1126/science.aab0751, 2015.

Fugal, J. P., Schulz, T. J., and Shaw, R. A.: Practical methods for automated reconstruction and characterization of particles in digital in-line holograms, Measurement Science and Technology, 20, 075501, https://doi.org/10.1088/0957-0233/20/7/075501, 2009.

Glienke, S., Kostinski, A. B., Shaw, R. A., Larsen, M. L., Fugal, J. P., Schlenczek, O., and Borrmann, S.: Holographic Observations of Centimeter-Scale Nonuniformities within Marine Stratocumulus Clouds, Journal of Atmospheric Sciences, 77, 499–512, https://doi.org/10.1175/JAS-D-19-0164.1, 2020.

Schlenczek, O.: Airborne and ground-based holographic measurement of hydrometeors in liquid-phase, mixed-phase and ice clouds, Ph.D. thesis, Johannes Gutenberg-Universität Mainz, https://doi.org/10.25358/openscience-4124, 2018.

Schlenczek, O., Nordsiek, F., Brunner, C. E., Chávez-Medina, V., Thiede, B., Bodenschatz, E., and Bagheri, G.: Airborne measurements of turbulence and cloud microphysics during PaCE 2022 using the Advanced Max Planck CloudKite Instrument (MPCK+), Earth System Science Data Discussions, 2025, 1–29, 2025.